Improved Continuous Fault Ride Through Control Strategy of DFIG-Based Wind Turbine During Commutation Failure in the LCC-HVDC Transmission System

Tian Zhang, Jun Yao, *Member, IEEE*, Peng Sun, Jinxin Pei, Hailin Zhang, *Member, IEEE*, Kai Liu, and Yang Zhao

***Abstract*—The commutation failure fault usually occurs in the line-commutated-converter-based high-voltage direct current transmission system. When commutation failure fault occurs, the voltage of sending alternate current (ac) system changes rapidly, and the connected doubly fed induction generator (DFIG)-based wind turbine may be tripped. Thus, the fault ride through (FRT) control strategy of DFIG should be investigated for enhancing the stability of the sending ac system. However, the voltage of the sending ac system during commutation failure is not changed in rectangular in shape, besides, the voltage presents the "first reduce then rise" characteristic, which is not considered in the existing FRT control strategies. In order to realize the continuous FRT of DFIG during commutation failure, the stator flux and electromotive force when the stator voltage changes continuously have been analyzed for the first time in this article. Furthermore, based on the analysis results, an improved continuous FRT control strategy is proposed. The simulation and experiment results validate the effectiveness of the proposed method. The proposed control strategy is not only suitable for the commutation failure condition, but also for the scenario with continuous voltage variation during grid fault, which indicates that the proposed method is general.**

***Index Terms*—Commutation failure, doubly fed induction generator (DFIG)-based wind turbine, improved continuous fault ride through control, line-commutated-converter-based high-voltage direct current (LCC-HVdc) transmission system, wind power generation.**

Manuscript received December 27, 2019; revised April 22, 2020; accepted May 29, 2020. Date of publication June 7, 2020; date of current version September 4, 2020. This work was supported in part by the National Natural Science Foundation of China under Grant 51977019, in part by the Joint Research Fund in Smart Grid (U1966208) under cooperative agreement between the National Natural Science Foundation of China and State Grid Corporation of China, in part by the 111 Project of China under Grant B18062, and in part by the Natural Science Foundation of Chongqing, China, under Grant cstc2019jcyj-bshX0050. Recommended for publication by Associate Editor M. S. ElMoursi. *(Corresponding author: Jun Yao.)*

The authors are with the State Key Laboratory of Power Transmission Equipment & System Security and New Technology, School of Electrical Engineering, Chongqing University, Chongqing 400044, China (e-mail: eemasterzhang@163.com; jyao@cqu.edu.cn; wdfasfe@qq.com; peijinxindoc@163.com; zhanghailin0310@sina.com; 760811938@qq.com; zhao_yang2080@yeah.net).

Color versions of one or more of the figures in this article are available online at https://ieeexplore.ieee.org.

Digital Object Identifier 10.1109/TPEL.2020.3000515

NOMENCLATURE

$P_{\rm ac}$, $Q_{\rm ac}$	Active and reactive power exchanged between the LCC-HVdc transmission system and the sending ac system.
$P_{\rm dc}$, $Q_{\rm dc}$	Transmitted active power and the consumed reactive power of the rectifier station.
$\boldsymbol{U}_r$, $\boldsymbol{U}_i$	Internal voltage vector of the sending ac system and the receiving ac system.
Z_r, Z_i	Internal impedance of the sending ac system and the receiving ac system
U_{dr}, U_{di}	DC voltage of the rectifier station and the inverter station.
$I_{\rm rd\_ref}$, I_d	DC current reference value and actual value.
α_r, α_i	Firing angles of the rectifier station and the inverter station.
U_1	Voltage amplitude of the rectifier station under no-load condition.
X_r	Commutation reactance.
B_c	Equivalent susceptance of the installed VAR compensation.
$\boldsymbol{U}_s$, U_s	Stator voltage vector and amplitude of DFIG.
$U_{r\max}$	Maximum rotor voltage of DFIG.
$I_{r\max}$	Maximum rotor current of DFIG.
$\boldsymbol{i}_{r\rm ref}$	Rotor current reference of DFIG.
φ, ω_s	Initial phase angle and electrical angular frequency of the stator voltage of DFIG.
T_s	Fundamental frequency period.
$\boldsymbol{i}_s$, i_s	Stator current vector and amplitude of DFIG.
$\boldsymbol{i}_r$, i_r	Rotor current vector and amplitude of DFIG.
$\boldsymbol{\psi}_s$	Stator flux of DFIG.
$\boldsymbol{\psi}_{s\rm dc}$	Stator transient dc flux of DFIG.
R_s, R_r	Stator resistance and rotor resistance of DFIG.
τ	Decaying rate of stator transient dc flux.
s	Slip of DFIG
L_s, L_m	Stator inductance and magnetizing inductance of DFIG.
σL_r	Rotor leakage inductance of DFIG.
$\boldsymbol{E}_r$	EMF vector of DFIG.

$\boldsymbol{u}_r$	Rotor voltage vector of DFIG.
L_{RSC}, k_r	Control coefficients of the inductance-emulating control strategy and the scaled current tracking control strategy.
k_{de}	Demagnetizing coefficient.
K_{p_r}, K_{i_r}	Proportion and integral coefficients of the constant-current controller in the rectifier station.
Superscript "*s*"	Static reference frame.
Superscript "*r*"	Rotor speed reference frame.
Subscript "*s*"	Stator variables of DFIG.
Subscript "*r*"	Rotor variables of DFIG.
Subscript "*d*, *q*"	*d*- and *q*-axis variables in the synchronous rotating reference frame.

I. Introduction

NOWADAYS, the doubly fed induction generator (DFIG)-based wind farm is becoming a trend over the decades. However, the wind power resources are generally located in the remote areas. The line commutated converter (LCC)-based high voltage direct current (HVdc) transmission system is used to transmit the large-scale wind power for the advantages of economy and technology in bulk power transmission over long distances and the fast power regulation ability [1]–[2].

Commutation failure is the frequent dynamic event in the LCC-HVdc transmission system [3], [4]. Moreover, the commutation failure fault is recoverable in a short time, which is different from the LCC-HVdc system blocking. Thus, the devices installed in the LCC-HVdc transmission system and the sending ac system are not allowed to be removed during commutation failure [5]. However, since the stator is directly connected with the power grid, the DFIG is very sensitive to the voltage disturbances [6]. During commutation failure, the stator voltage of DFIG changes rapidly, which may introduce the overcurrent of the rotor-side converter (RSC).

In order to prevent the commutation failure fault, research studies have been presented in the past decades, and various approaches have been developed. These proposed methods can be classified into two main categories: auxiliary hardware method, and improved control strategy [7], [8].

In the first category, many research studies focus on the capacitor commutated converter (CCC) and proposed different topologies to eliminate the commutation failure [9]–[11]. However, the voltage stress of the thyristor valves in the CCC is significantly increased, which will shorten the lifetime. Furthermore, the CCC will increase the costs inevitably. Therefore, the CCC-HVdc transmission system is not widely used in the actual HVdc project [12]. Additionally, the dynamic reactive power compensator, such as static synchronous compensator and synchronous condenser are also proposed to suppress commutation failure in the inverter station [13], [14].

As for the second category, the objective of the improved control strategy is to increase the commutation margin by advancing the firing angle during fault. For example, a fuzzy controller is designed in [15] to regulate the firing angle of the inverter station during fault automatically. Meanwhile, considering the direct current variation in the presence of system disturbances, Wei *et al.* [16] developed a direct-current predictive control strategy based on commutation failure prevention mechanism proposed in [17] and [18]. Moreover, Mirsaeidi and Dong [19] proposed a commutation failure mitigation algorithm, in which the overlap area of thyristor is measured directly to modify the firing angle of the inverter station. Although there are many improved control strategies, the commutation failure fault cannot be completely eliminated in the LCC-HVdc transmission system [9].

In order to enhance the stability of the sending ac system during commutation failure, the fault ride through (FRT) of DFIG-based wind turbine is necessary. The existing FRT control strategies of DFIG can be classified into two categories, namely, the auxiliary hardware methods and the improved control strategies [20]. The crowbar circuit is the mostly used auxiliary hardware for its simple and reliable features. However, when the crowbar circuit is activated during fault, the RSC will lose its control and the DFIG will absorb reactive power from the grid, which may further worsen the voltage of the connected power grid. Meanwhile, the auxiliary hardware will undoubtedly increase the costs.

Furthermore, the improved control strategies of DFIG during fault have been proposed over the decades for overcoming the disadvantages of the auxiliary hardware method. However, the existing FRT control strategies of DFIG do not consider the special characteristics of voltage in the sending ac system during commutation failure.

When commutation failure occurs in the LCC-HVdc transmission system, the stator voltage changes continuously and fits "voltage drop–voltage rise–voltage recovery" pattern. Therefore, in order to realize the commutation failure FRT of DFIG, the control strategy should be suitable for both the stator voltage drop and the stator voltage swell. However, the existing control strategies only considered the low-voltage ride through (LVRT) or high-voltage ride through (HVRT). For example, several LVRT control strategies, including "demagnetizing control strategy," "inductance-emulating control strategy," "scaled current tracking control strategy," and "virtual damping flux control strategy," are proposed in [21]–[24]. In addition, the HVRT control strategies, including "virtual impedance control strategy" and "dynamic reactive power injection control strategy," are proposed in [25] and [26]. Additionally, all the existing control strategies are based on the typical rectangular change pattern of stator voltage of DFIG during fault, i.e., the stator voltage under fault can be divided into three parts, namely, prefault steady state, fault steady state, and postfault steady state [27]. In other words, the dynamic process of the voltage change during fault is ignored. However, the stator voltage changes continuously and rapidly during commutation failure. Consequently, the dynamic process of the voltage change cannot be ignored, which is completely different from the mostly research situation. Therefore, it is necessary to investigate the continuous FRT control strategy of DFIG.

This article studies the improved continuous FRT control strategy of DFIG without auxiliary devices, which means that the rotor overcurrent of DFIG should be restricted under the control of RSC during fault. Compared with the existing methods, for

realizing the continuous FRT of DFIG, there are four major works presented in this article listed as follows:

1) the model of stator voltage during commutation failure is proposed;
2) the stator flux and electromotive force (EMF) when the stator voltage changes continuously are analyzed for the first time;
3) the limitation of the existing FRT control strategies is researched;
4) the continuous FRT control strategy is proposed, and the control coefficient of the proposed strategy is designed.

Compared with the existing FRT control strategies, the proposed continuous FRT control strategy has some advantages, including the overcurrent suppression ability of DFIG that can be further improved under the stator voltage continuous changing condition. Besides, the control coefficient can be chosen reasonably according to the operation status of the DFIG system. Thus, the transient dc flux can be decayed rapidly, and the DFIG can provide dynamic reactive current to support the connected power grid, which means that the DFIG system can operate more flexible and the performance of FRT can be enhanced. Furthermore, the proposed continuous FRT control strategy is general to the scenarios with the continuous voltage variation condition.

The rest of this article is organized as follows. Section II analyzed the commutation failure process and the stator voltage of DFIG under typical LCC-HVdc commutation failure fault. Meanwhile, the model of the commutation failure voltage is proposed in Section III. Section IV proposed the continuous FRT control strategy. Sections V and VI present the simulation and experimental verifications of the proposed control strategy, respectively. Based on the simulation and experiment, the proposed continuous FRT control strategy is well demonstrated. Finally, Section VII concludes this article.

II. Stator Voltage Analysis During Commutation Failure

Referring to the CIGRE benchmark model of the HVdc transmission system [28], the bipolar LCC-HVdc transmission system is built in Matlab/Simulink. Besides, a 100-MW DFIG-based wind farm is installed in the sending ac system to analyze the voltage characteristics during commutation failure. The configuration of the simulation system is shown in Fig. 1, and the parameters are listed in the Appendix. According to Wang *et al.* [29], the main reasons for commutation failure fault include the following:

1) loss of the trigger pulse;
2) the commutation voltage drops significantly or the increase in dc current is too large;
3) the extinguishing angle of the inverter station is too small;
4) the zero crossing of the commutation voltage forward.

In this article, the simulation results shown in Figs. 3 and 4 are caused by the loss of trigger pulse in the inverter station. During the simulation, the thyristor valve of the upper arm of phase B in the inverter station is set to lose the trigger pulse at $t = 2$ s and then to recover to the normal operation. The voltage

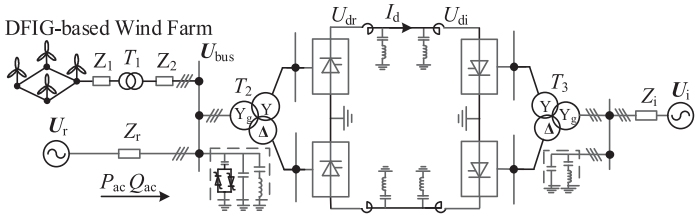

Fig. 1. Configuration of bipolar LCC-HVdc transmission system.

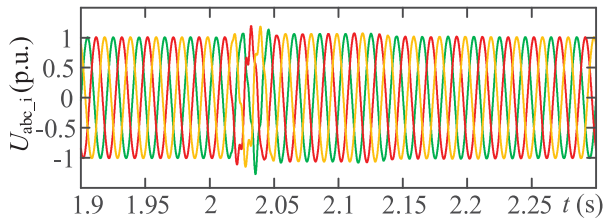

Fig. 2. Voltage waveform at inverter side during commutation failure.

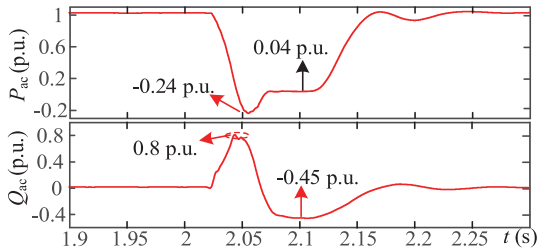

Fig. 3. Active power and reactive power exchanged between the LCC-HVdc transmission system and the sending ac system during commutation failure.

waveform at inverter side during commutation failure is given in Fig. 2. The active power and reactive power exchanged between the LCC-HVdc transmission system and the sending ac system during commutation failure is shown in Fig. 3. Furthermore, the waveforms of the dc voltage, dc current, and firing angle of the positive pole of converter station during commutation failure are shown in Fig. 4. The stator voltage rms of DFIG-based wind turbine is shown in Fig. 5. Additionally, $P_{\rm dc}$ and $Q_{\rm dc}$ based on the quasi-steady-state mathematical model of the bipolar LCC-HVdc transmission system are expressed in (1) and (2), respectively [30]

$$Q_{\rm dc} = P_{\mathbf{dc}} \times \tan\left\{\arccos\left(\cos\alpha_r - \frac{X_{r\mathbf{1}} I_d}{\sqrt{2}U_1}\right)\right\} \quad (1)$$

$$P_{\rm dc} = 2 \times \left(\frac{6\sqrt{2}}{\pi} U_1 \cos\alpha_r - \frac{6}{\pi} X_{r\mathbf{1}} I_d\right) I_d. \quad (2)$$

According to the simulation results shown in Fig. 4, the typical commutation failure process is presented as follows. The dc voltage of the inverter station drops when commutation failure fault occurs at $t = 2.02$ s, which leads to the increase in dc current. After $t = 2.02$ s, under the control of the constant-current regulator of the rectifier station and the constant voltage regulator of the inverter station, α_r and α_i will increase for decreasing the dc

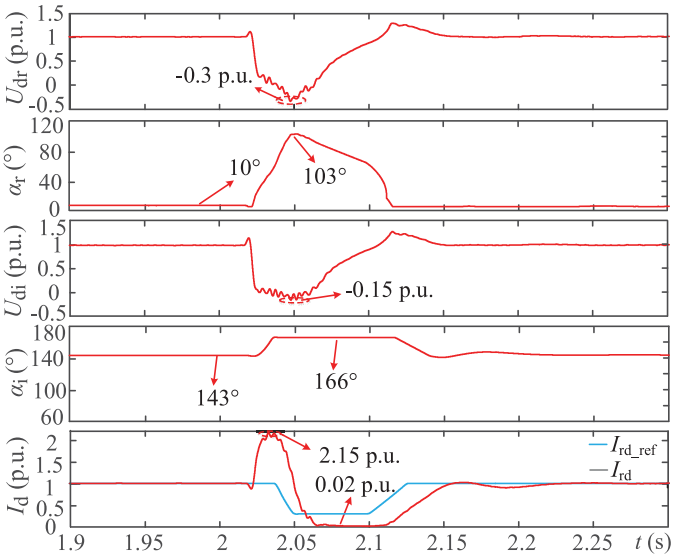

Fig. 4. Signals of the LCC-HVdc during commutation failure.

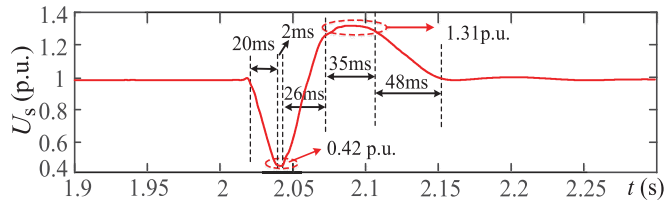

Fig. 5. Stator voltage rms of DFIG during commutation failure.

current, which makes α_i rapidly reach the upper limitation value of firing angle. Then, after $t = 2.04$ s, the dc current decreases fast until the dc current nearly equals 0 p.u. At $t = 2.0522$ s, the α_r starts to decrease for increasing the dc current, whereas α_i is still equal to the upper limitation value of firing angle. The dc current gradually returns to the rated value after 2.11 s. Finally, the LCC-HVdc transmission system recovers to normal operation at $t = 2.161$ s.

Based on the commutation failure process and $Q_{\rm dc}$, and $P_{\rm dc}$ shown in (1) and (2), respectively, the pattern of the stator voltage change during commutation failure is analyzed as follows.

When the LCC-HVdc transmission system operates under the normal condition, the reactive power that the rectifier station consumed is balanced by the VAR compensators [31]. Thus, there is no reactive power exchange between the sending ac system and the LCC-HVdc transmission system. When the commutation failure fault occurs in the inverter station, the α_r increases rapidly after I_d rises, which leads to the decrease in U_{dr}. As a result, the transmitted active power decreases. In addition, the transmitted active power is even negative when $\alpha_r > 90°$. However, the consumed reactive power of the rectifier station increases for the increase in α_r and I_d. Therefore, the LCC-HVdc transmission system absorbs a large amount of reactive power from the sending ac system, which leads to the stator voltage of DFIG drops rapidly. Afterward, the I_d decreases under the control of the rectifier station and the inverter station. As a result, the reactive power that the rectifier station consumed

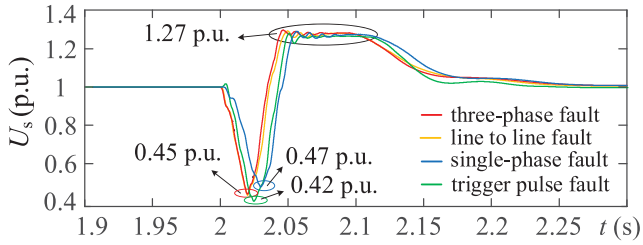

Fig. 6. Stator voltage rms of DFIG during commutation failure under different types of fault.

gradually decreases, and the stator voltage swells. When I_d is close to 0 p.u., the transmitted active power and the consumed reactive power of the rectifier station are approximately equal to 0 p.u. Besides, the stator voltage is up to 1.31 p.u. in the studied system. Then, the stator voltage gradually returns to the rated value when the normal operation of the LCC-HVdc transmission system is recovered.

The typical single-phase fault, three-phase fault, line-to-line fault, and trigger pulse fault in the receiving ac system have been simulated under the same conditions. During the simulation, the faults in the receiving ac system occur at $t = 2$ s and recover at $t = 2.05$ s. The simulation results are given in Fig. 6. It can be seen from Fig. 6 that the peak values and the minimum values of stator voltage under different types of fault are close to each other. Meanwhile, the ramping rate of stator voltage under three-phase fault is largest, whereas the ramping rate under single-phase fault is smallest.

Although the stator voltage shapes under different types of fault have some differences, the stator voltages during commutation failure present the "first reduce then rise" characteristic and change continuously. In this article, the commutation failure voltage caused by loss of trigger pulse in the inverter station is taken as an example to investigate the continuous FRT control strategy of DFIG.

III. Model of Stator Voltage During Commutation Failure

According to Fig. 5, the stator voltage rms during commutation failure can be divided into five periods, namely, the voltage decrease period, the low-voltage duration period, the voltage increase period, the high-voltage duration period, and the voltage recovery period. Meanwhile, the voltage of different periods can be approximately fitted with straight lines. Since the low-voltage duration period is rather short, which can be reasonably neglected. Consequently, the stator voltage rms during commutation failure can be presented as four periods except for the low-voltage duration period. The fitting line result of Fig. 5 is shown in Fig. 7. In Fig. 7, the voltage of high-voltage duration period is fitted as a straight line with zero slope, whereas the other periods are fitted as straight lines with constant slope.

In Fig. 7, t_1, t_2, t_3, t_4, and t_5 are the interval points of different periods.

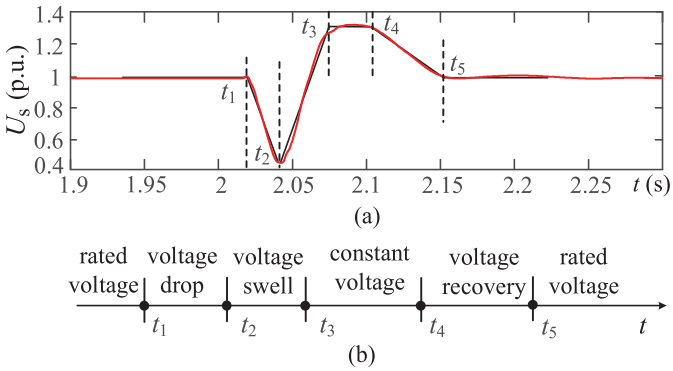

Fig. 7. Fitting result of stator voltage rms during commutation failure. (a) The fitting result of stator voltage rms. (b) The time sequence diagram of fitting result.

Based on the fitting results shown in Fig. 7, the model of stator voltage during commutation failure can be described as

$$\boldsymbol{U}_s^s = \begin{cases} \boldsymbol{U}_s^s & t < t_1 \\ [1 - k_1(t - t_1)] \times \boldsymbol{U}_s^s & t_1 \le t < t_2 \\ [\mu_1 + k_2(t - t_2)] \times \boldsymbol{U}_s^s & t_2 \le t < t_3 \\ \mu_2 \times \boldsymbol{U}_s^s & t_3 \le t < t_4 \\ [\mu_2 - k_3(t - t_4)] \times \boldsymbol{U}_s^s & t_4 \le t < t_5 \\ \boldsymbol{U}_s^s & t_5 \le t \end{cases} \tag{3}$$

where k_1, k_2, and k_3 are the slopes of the fitting straight lines of different periods. μ_1 and μ_2 are the minimum value and maximum value of stator voltage during commutation failure, respectively. In the following analysis, $f_1(t)$, $f_2(t)$, and $f_3(t)$ are used to, respectively, replace the terms $[1 - k_1(t - t_1)]$, $[\mu_1 + k_2(t - t_2)]$, and $[\mu_2 + k_3(t - t_4)]$.

According to (3), the stator flux of DFIG is deduced as (4) when the stator resistance is neglected.

In (4), $\boldsymbol{C}_1$, $\boldsymbol{C}_2$, $\boldsymbol{C}_3$, $\boldsymbol{C}_4$, and $\boldsymbol{C}_5$ are the initial vectors of $\boldsymbol{\psi}_{\text{sdc}}^s$ during different commutation failure periods, which can be written as (5)

$$\boldsymbol{\psi}_s^s = \begin{cases} \frac{\boldsymbol{U}_s^s}{j\omega_s} & t < t_1 \\ \frac{f_1(t)\times\boldsymbol{U}_s^s}{j\omega_s} - \frac{k_1\times\boldsymbol{U}_s^s}{\omega_s^2} + \boldsymbol{C}_1 \times e^{\frac{-(t-t_1)}{\tau}} & t_1 \le t < t_2 \\ \frac{f_2(t)\times\boldsymbol{U}_s^s}{j\omega_s} + \frac{k_2\times\boldsymbol{U}_s^s}{\omega_s^2} + \boldsymbol{C}_2 \times e^{\frac{-(t-t_2)}{\tau}} & t_2 \le t < t_3 \\ \frac{\mu_2\times\boldsymbol{U}_s^s}{j\omega_s} + \boldsymbol{C}_3 \times e^{\frac{-(t-t_3)}{\tau}} & t_3 \le t < t_4 \\ \frac{f_3(t)\times\boldsymbol{U}_s^s}{j\omega_s} - \frac{k_3\times\boldsymbol{U}_s^s}{\omega_s^2} + \boldsymbol{C}_4 \times e^{\frac{-(t-t_4)}{\tau}} & t_4 \le t < t_5 \\ \frac{\boldsymbol{U}_s^s}{j\omega_s} + \boldsymbol{C}_5 \times e^{\frac{-(t-t_5)}{\tau}} & t_5 \le t \end{cases} \tag{4}$$

$$\begin{cases} \boldsymbol{C}_1 = 0 & t_1 \le t < t_2 \\ \boldsymbol{C}_2 = \boldsymbol{C}_1 \times e^{\frac{-(t_2-t_1)}{\tau}} - \frac{k_1+k_2}{\omega_s^2} U_s e^{j(\omega_s t_2+\varphi)} + \frac{k_1\times U_s e^{j(\omega_s t_1+\varphi)}}{\omega_s^2} & t_2 \le t < t_3 \\ \boldsymbol{C}_3 = \boldsymbol{C}_2 \times e^{\frac{-(t_3-t_2)}{\tau}} + \frac{k_2\times U_s e^{j(\omega_s t_3+\varphi)}}{\omega_s^2} & t_3 \le t < t_4 \\ \boldsymbol{C}_4 = \boldsymbol{C}_3 \times e^{\frac{-(t_4-t_3)}{\tau}} + \frac{k_3\times U_s e^{j(\omega_s t_4+\varphi)}}{\omega_s^2} & t_4 \le t < t_5 \\ \boldsymbol{C}_5 = \boldsymbol{C}_4 \times e^{\frac{-(t_5-t_4)}{\tau}} - \frac{k_3\times U_s e^{j(\omega_s t_5+\varphi)}}{\omega_s^2} & t_5 \le t. \end{cases} \tag{5}$$

In (5), the flux can be divided into two parts. The first part is the stator transient dc flux of the previous period, whereas the second part is the stator transient dc flux generated in the current period. Since the stator transient dc flux is the sum of the transient dc flux vectors generated in the previous period and the current period, it can be considered that the stator transient dc flux is accumulated when the stator voltage changes continuously.

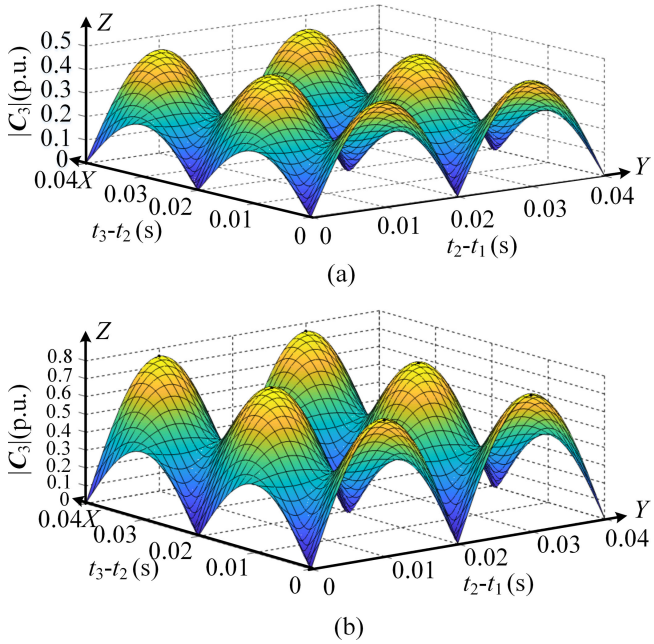

Fig. 8. Initial amplitude of stator transient dc flux during high-voltage duration. (a) $k_1 = k_2 = 35$. (b) $k_1 = k_2 = 60$.

Because $\boldsymbol{\psi}_{\text{sdc}}^s$ is accumulated, both the duration time of different periods and the slopes of stator voltage change are the key factors to $|\boldsymbol{\psi}_{\text{sdc}}|$. For example, Fig. 8 shows the initial amplitude of $|\boldsymbol{\psi}_{\text{sdc}}|$ of the high-voltage duration period based on (5). In Fig. 8, the Z-axis is the initial amplitude of $|\boldsymbol{C}_3|$, the X-axis is the duration time of voltage increase period, and the Y-axis is the duration time of voltage decrease period. Moreover, in Fig. 8(a), $k_1 = k_2 = 35$, whereas in Fig. 8(b) $k_1 = k_2 = 60$.

From Fig. 8, $|\boldsymbol{C}_3|$ is nearly equal to 0 p.u. when the duration time of both the two periods are equal to the integer multiple of T_s, whereas $|\boldsymbol{C}_3|$ has the maximum value when the duration time of both the two periods are equal to the integer multiple of $0.5 \times T_s$. Moreover, in Fig. 8(a) and (b), the maximum values of $|\boldsymbol{C}_3|$ are 0.441 p.u. and 0.752 p.u., respectively, which indicates that the large slopes of stator voltage change will lead to a large $|\boldsymbol{\psi}_{\text{sdc}}|$ during commutation failure.

The control coefficients of the constant-current controller in the rectifier station will influence the ramping rate of commutation failure voltage, and then the ramping rate of stator voltage during the fault will be affected as well. The simulation results of stator voltage under different control coefficients of the constant-current controller in the rectifier station are given in Fig. 9. It can be seen from Fig. 9, the increase in control coefficients will accelerate the ramping rate of stator voltage when the commutation failure occurs. Furthermore, according to the analysis mentioned above, the ramping rate of stator voltage has a great influence on DFIG. Meanwhile, the larger the ramping rate of stator voltage, the greater the influence on the operation of DFIG. Consequently, in this article, the slight

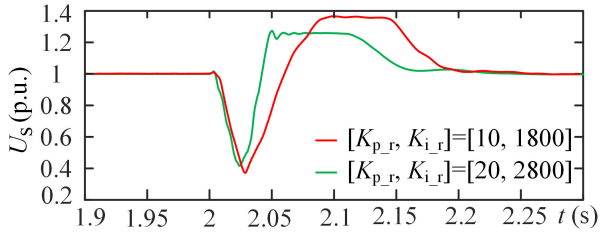

Fig. 9. Stator voltage during commutation failure with different control coefficients of the constant-current controller in the rectifier station.

commutation failure and the severe commutation failure are defined respectively. The difference between slight commutation failure and severe commutation failure is that the ramping rate of commutation failure voltage is different. The ramping rate of commutation failure voltage during the severe commutation failure is significantly larger than that during the slight commutation failure.

In this article, the slight commutation failure is simulated by setting $k_1 = k_2 = 35$, $k_3 = 15$, $\mu_1 = 0.4$ p.u., $\mu_2 = 1.3$ p.u., and $t_4 - t_3 = 40$ ms, whereas the severe commutation failure is simulated by setting $k_1 = k_2 = 60$, $k_3 = 15$, $\mu_1 = 0.4$ p.u., $\mu_2 = 1.3$ p.u., and $t_4 - t_3 = 40$ ms for validating the effectiveness of the proposed continuous FRT control strategy.

In the following sections, theoretical analysis of the stator flux is based on the analytical expression of stator flux given in this section.

IV. Continuous Fault Ride Through Control Strategy

The stator voltage of DFIG during commutation failure has prominent differences from the voltage of other faults, which is not considered in the existing research works. In order to enhance the stability of the sending ac system during commutation failure, this article proposed a continuous FRT control strategy of DFIG based on the stator voltage characteristics during commutation failure.

A. EMF Characteristics Analysis of DFIG Under Fault

Based on the analysis mentioned above, the stator voltage changes continuously during commutation failure, and the dynamic process of the voltage change cannot be ignored. Therefore, in this article, the stator voltage vector for considering the dynamic process of the voltage variation during fault is expressed as follows:

$$\boldsymbol{U}_s^s = h(t) \times U_s e^{j(\omega_s t+\varphi)} \tag{6}$$

where $h(t)$ is a continuous function, which represents the characteristics of the stator voltage of DFIG.

According to (6), the stator flux when the stator voltage changes continuously can be presented as

$$\boldsymbol{\psi}_s^s = \frac{h(t)}{j\omega_s} \times U_s e^{j(\omega_s t+\varphi)} - \int \frac{h'(t)}{j\omega_s} \times U_s e^{j(\omega_s t+\varphi)} dt + \boldsymbol{\psi}_{sdc}^s e^{-t/\tau} \tag{7}$$

where $h'(t)$ is the derivative of $h(t)$ with respect to t.

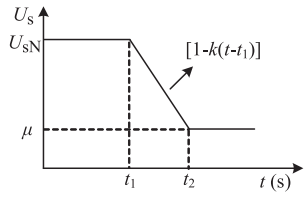

Fig. 10. Stator voltage magnitude.

From (7), the stator flux can be classified into three components presented as $\boldsymbol{\psi}_{sa}^s$, $\boldsymbol{\psi}_{sb}^s$, and $\boldsymbol{\psi}_{sdc}^s$, respectively. The expressions of $\boldsymbol{\psi}_{sa}^s$ and $\boldsymbol{\psi}_{sb}^s$ are given as

$$\begin{cases} \boldsymbol{\psi}_{sa}^s = \frac{h(t)}{j\omega_s} \times U_s e^{j(\omega_s t+\varphi)} \\ \boldsymbol{\psi}_{sb}^s = -\int \frac{h'(t)}{j\omega_s} \times U_s e^{j(\omega_s t+\varphi)} dt. \end{cases} \tag{8}$$

According to (8), the amplitude of $\boldsymbol{\psi}_{sa}^s$ is proportional to $h(t)$, whereas the amplitude of $\boldsymbol{\psi}_{sb}^s$ is decided by $h'(t)$. When $h'(t)$ is equal to 0, i.e., the stator voltage amplitude is constant, the amplitude of $\boldsymbol{\psi}_{sb}^s$ is equal to 0 p.u. as well. $\boldsymbol{\psi}_{sb}^s$ is the term that is ignored during fault in the existing researches. It can be noted that $\boldsymbol{\psi}_{sb}$ and $\boldsymbol{\psi}_{sdc}$ have the same order of magnitude, which can be illustrated as follows.

The stator flux when the stator voltage changes, as shown in Fig. 10, is given as

$$\boldsymbol{\psi}_s^s = \begin{cases} \frac{\boldsymbol{U}_{sN}^s}{j\omega_s} & t<t_1 \\ \frac{f(t)\times\boldsymbol{U}_{sN}^s}{j\omega_s} - \frac{k\times\boldsymbol{U}_{sN}^s}{\omega_s^2} + \frac{k\times U_{sN}^s e^{j(\omega_s t_1+\varphi)}}{\omega_s^2} \times e^{\frac{-(t-t_1)}{\tau}} & t_1 \le t < t_2 \\ \frac{\mu\times\boldsymbol{U}_{sN}^s}{j\omega_s} + \frac{k\times U_{sN}^s e^{j(\omega_s t_1+\varphi)}}{\omega_s^2} \times e^{\frac{-(t-t_1)}{\tau}} & t_2 \le t \end{cases} \tag{9}$$

where $f(t)$ is used to replace the $[1 - k(t - t_1)]$.

Based on (9), when $t_1 \le t < t_2$, $|\boldsymbol{\psi}_{sb1}|$ and $|\boldsymbol{\psi}_{sdc1}|$ are shown in (10). It can be seen from (10) that $\boldsymbol{\psi}_{sb1}$ and $\boldsymbol{\psi}_{sdc1}$ have the same order of magnitude when stator voltage changes, as shown in Fig. 10. Since the different stator voltage shapes can be fitted with the voltage shown in Fig. 10, $\boldsymbol{\psi}_{sb}$ and $\boldsymbol{\psi}_{sdc}$ have the same order of magnitude during fault

$$\begin{cases} |\boldsymbol{\psi}_{sb1}^s| = k \times U_{sN}^s / \omega_s^2 \\ |\boldsymbol{\psi}_{sdc1}^s| = k \times U_{sN}^s e^{\frac{-(t-t_1)}{\tau}} \Big/ \omega_s^2. \end{cases} \tag{10}$$

Additionally, the rotor EMF under static reference frame can be presented as (11) according to the model of DFIG

$$\boldsymbol{E}_r^s = \frac{L_m}{L_s} e^{j\omega_r t} \times \left[\frac{d\boldsymbol{\psi}_s^s}{dt} e^{-j\omega_r t} - j\omega_r e^{-j\omega_r t} \times \boldsymbol{\psi}_s^s \right]. \tag{11}$$

According to (7) and (11), when the stator voltage changes continuously, the rotor EMF under static reference frame can be expressed as

$$\boldsymbol{E}_r^s = \frac{L_m}{L_s} \times \left[sh(t) U_s e^{j(\omega_s t+\varphi)} + j\omega_r \int \frac{h'(t)}{j\omega_s} U_s e^{j(\omega_s t+\varphi)} dt - \left(j\omega_r + \frac{1}{\tau} \right) \boldsymbol{\psi}_{sdc}^s \right]. \tag{12}$$

As mentioned in [19], since $1/\tau$ is much less than ω_r, (12) can be further simplified as

$$\boldsymbol{E}_r^s = \frac{L_m}{L_s}[s \times h(t) \times e^{j(\omega_s t+\varphi)} + (1-s) \times \int h'(t) e^{j(\omega_s t+\varphi)} dt - j(1-s) \times \omega_s \times \boldsymbol{\psi}_{sdc}^s]. \quad (13)$$

According to (7) and (13), the relation between stator flux and the EMF during fault is illustrated as follows:

$$\begin{cases} \boldsymbol{E}_{ra}^s &= j\frac{L_m}{L_s} s\omega_s \times \boldsymbol{\psi}_{sa}^s \\ \boldsymbol{E}_{rb}^s &= -j\frac{L_m}{L_s}(1-s)\omega_s \times \boldsymbol{\psi}_{sb}^s \\ \boldsymbol{E}_{rdc}^s &= -j\frac{L_m}{L_s}(1-s)\omega_s \times \boldsymbol{\psi}_{sdc}^s. \end{cases} \quad (14)$$

Based on (14), the coefficient between $\boldsymbol{\psi}_{\mathrm{sb}}^s$ and $\boldsymbol{E}_{rb}^s$ is the same as the coefficient between $\boldsymbol{\psi}_{\mathrm{sdc}}^s$ and $\boldsymbol{E}_{rdc}^s$. That is to say, $\boldsymbol{\psi}_{\mathrm{sb}}^s$ and $\boldsymbol{\psi}_{\mathrm{sdc}}^s$ have the same contribution to the EMF. Thus, both $\boldsymbol{\psi}_{\mathrm{sb}}^s$ and $\boldsymbol{\psi}_{\mathrm{sdc}}^s$ should be well controlled during fault. In this article, the sum of $\boldsymbol{\psi}_{\mathrm{sb}}^s$ and $\boldsymbol{\psi}_{\mathrm{sdc}}^s$ is defined as $\boldsymbol{\psi}_{\mathrm{st}}^s$, as follows

$$\boldsymbol{\psi}_{st}^s = \boldsymbol{\psi}_{sb}^s + \boldsymbol{\psi}_{sdc}^s. \quad (15)$$

It is worth noting that the waveform of $h(t)$ is not defined in (6). Therefore, the analysis in this section is not only applicable to the commutation failure, but also applicable to the scenario with continuous voltage variation.

B. Analysis of the Limitation of the Existing FRT Control Strategies

Many FRT control strategies of DFIG have been proposed in the past decades. However, the existing FRT control strategies cannot been adopted directly for realizing the continuous FRT of DFIG during commutation failure.

The literature [21] proposed a demagnetizing control strategy, which introduced $\boldsymbol{\psi}_{\mathrm{sdc}}^s$ into the rotor current reference to suppress the overcurrent of DFIG rotor during fault. The rotor current reference and the calculated rotor voltage of the demagnetizing control strategy are shown in (16). According to (16), the demagnetizing control strategy must measure $\boldsymbol{\psi}_{\mathrm{sdc}}^s$ in real time, and the mostly used measurement method of $\boldsymbol{\psi}_{\mathrm{sdc}}^s$ is shown in Fig. 11. During the initial stage of stator voltage drop fault, the stator flux contains the fundamental frequency component and the transient dc component. Therefore, the measurement method shown in Fig. 11 can measure $\boldsymbol{\psi}_{\mathrm{sdc}}^s$ accurately. However, if the stator voltage changes continuously, the amplitude of stator flux will change continuously as well according to (7). Consequently, the stator flux contains not only the fundamental frequency component and the transient dc component, but also another series of frequency components. Since the bandpass filter has a poor attenuation ability of the harmonic frequency components, it is difficult to measure $\boldsymbol{\psi}_{\mathrm{sdc}}^s$ accurately and quickly with the traditional bandpass filter method when the stator voltage changes continuously

$$\begin{cases} \boldsymbol{i}_{\mathrm{rref}}^r = -k_{\mathrm{de}} \times \boldsymbol{\psi}_{sdc}^r \\ \boldsymbol{u}_r^r = \left(\frac{L_m}{L_s} - \sigma L_r k_{de}\right) \times \frac{d}{dt}\boldsymbol{\psi}_{sdc}^r + \frac{L_m}{L_s} \times \frac{d}{dt}\boldsymbol{\psi}_{sa}^r \end{cases} \quad (16)$$

where k_{de} is the demagnetizing coefficient.

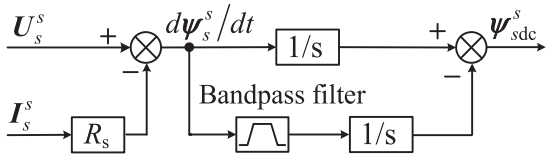

Fig. 11. Schematic diagram of the transient dc stator flux measurement.

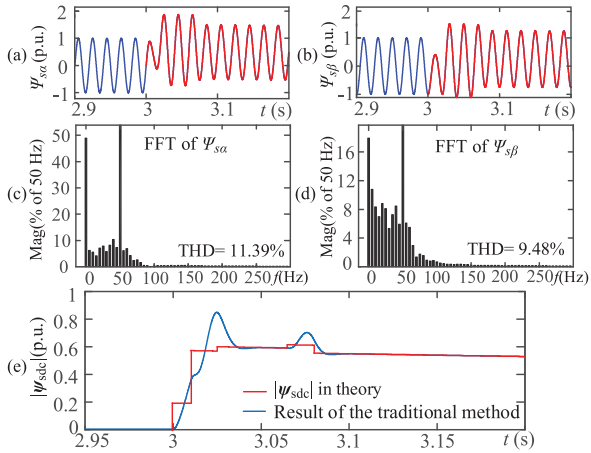

Fig. 12. (a) and (b) Stator flux in the stationary frame during severe commutation failure. (c) and (d) FFT results of stator flux. (e) Measurement results of the transient dc flux with the method shown in Fig. 11.

Based on the method shown in Fig. 11, Fig. 12 shows the fast Fourier transform (FFT) result of the stator flux and the measurement result of $|\psi_{\mathrm{sdc}}|$ under severe commutation failure. As can be seen, the stator flux contains many low-frequency harmonics during the fault. Consequently, $\boldsymbol{\psi}_{\mathrm{sdc}}^s$ is hard to measure accurately and quickly with the existing method, which will weaken the overcurrent suppression ability of the demagnetizing control strategy.

Additionally, according to the mathematical model of DFIG, FRT control strategies without the measurement of $\boldsymbol{\psi}_{\mathrm{sdc}}^s$ during fault have been studied as well, for example, the inductance-emulating control strategy [22] and the scaled current tracking control strategy [23]. In fact, when the control coefficients of the two control strategies accord with the ratio shown in (17), the rotor current reference as well as calculated rotor voltage of the two control strategies is same. Thus, these control strategies can be considered as equivalent in theory. In the following analysis, the inductance-emulating control strategy is taken as an example to study

$$L_{RSC} = \frac{L_s L_m - k_r L_m^2}{L_s k_r} - \sigma L_r. \quad (17)$$

The rotor current reference and the calculated rotor voltage of the inductance-emulating control strategy are given in (18). The range of L_{RSC} is given in (19) [22]

$$\begin{cases} \boldsymbol{i}_{\mathrm{rref}}^r = \frac{-L_m}{L_s(L_{RSC}+\sigma L_r)} \times \boldsymbol{\psi}_s^r = -k_L \times \boldsymbol{\psi}_s^r \\ \boldsymbol{u}_r^r = (\frac{L_m}{L_s} - \sigma L_r k_L) \times \frac{d}{dt}\boldsymbol{\psi}_s^r \end{cases} \quad (18)$$

where k_L is the equivalent demagnetizing coefficient

$$\begin{cases} L_{RSC\min} = \frac{L_m}{L_s|I_{rmax}|}|\psi_{smax}| - \sigma L_r \\ L_{RSC\max} = \frac{\sigma L_r |U_{rmax}|}{|E_{rmax}|-|U_{rmax}|}. \end{cases} \quad (19)$$

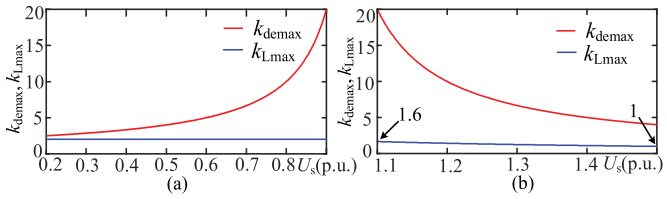

Fig. 13. Maximum demagnetizing coefficients of the demagnetizing control strategy and inductance-emulating control strategy with different fault degrees. (a) Stator voltage drop. (b) Stator voltage swell.

According to (18) and (19), the rotor current reference of the inductance-emulating control strategy is proportional to $|\psi_s|$, whereas the rotor current reference of the demagnetizing control strategy is proportional to $|\psi_{sdc}|$. As a result, in order to satisfy the rotor current constraint, a large L_{RSC}, namely, the little k_L, should be selected for realizing the continuous FRT of DFIG when the inductance-emulating control strategy is adopted. Compared with the inductance-emulating control strategy, k_{de} that is much bigger than k_L can be chosen with the demagnetizing control strategy. As a result, the calculated rotor voltage of the inductance-emulating control strategy is bigger than the demagnetizing control strategy, according to (16) and (18).

In order to illustrate the analysis mentioned above, k_{demax} and $k_{L\max}$ during fault are given in (20). Moreover, the curves of the k_{demax} and $k_{L\max}$ under stator voltage drop are given in Fig. 13(a), whereas the curves of the k_{demax} and $k_{L\max}$ under stator voltage swell are given in Fig. 13(b). In Fig. 13, the decay of the transient dc flux is ignored for the large stator time constant of DFIG under the rotor open-circuit condition. As can be seen from Fig. 13, $k_{L\max}$ is much less than k_{demax} under stator voltage swell. Since the continuous FRT control strategy should be suitable for both the stator voltage drop and the stator voltage swell condition, the little k_L should be chosen when the inductance-emulating control strategy is adopted, which indicates that the required rotor voltage of the inductance-emulating control strategy is much bigger than the demagnetizing control strategy. When the required rotor voltage exceeds the output voltage limitation of RSC, the rotor current is out of control and may bring security issues to the DFIG system. Therefore, the inductance-emulating control strategy has a weak ability to suppress the overcurrent for realizing the continuous FRT of DFIG

$$\begin{cases} k_{de\max} = \dfrac{|I_{rmax}|}{|\psi_{sdc}|} \\ k_{L\max} = \dfrac{|I_{rmax}|}{|\psi_s|}. \end{cases} \tag{20}$$

As can be seen from above-mentioned analysis, the existing FRT control strategies cannot be applied directly for realizing the continuous FRT of DFIG. Thus, in order to enhance the stability of the sending ac system, the continuous FRT control strategy should be investigated.

C. Continuous FRT Control Strategy of DFIG

The DFIG has a weak ability to suppress the overcurrent during continuous FRT when ψ_s is introduced into the rotor current reference. Moreover, ψ_{st} is the key factor to the rotor overcurrent during fault. Therefore, in order to make full use of the overcurrent suppression capability of DFIG and decay ψ_{sdc} rapidly, ψ_{st} is introduced into the rotor current reference in the proposed continuous FRT control strategy. The rotor current reference of the proposed method is given in (21), and the measurement method of ψ_{st} is illustrated in Fig. 14. Since the three-order harmonic components can be removed by the delta connection of the step-up transformer of DFIG, the cut-off frequency of the low-pass filter in the proposed measurement method for ψ_{st} is set up to 150 Hz to filter out the high-order harmonic components

$$\boldsymbol{i}^r_{\mathrm{rref}} = -k_{de}\boldsymbol{\psi}^r_{st}. \tag{21}$$

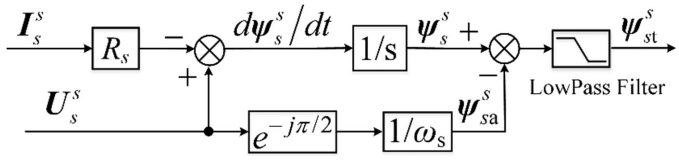

Fig. 14. Proposed measurement method for ψ_{st}.

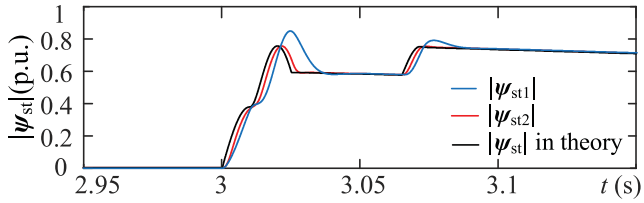

Fig. 15. Measurement results of the proposed measurement method during severe commutation failure.

Simulation has been done in Matlab/Simulink for validating the effectiveness of the proposed measurement method. The results of the traditional transient dc flux measurement method and the proposed measurement method presented as $|\psi_{\mathrm{st}1}|$ and $|\psi_{\mathrm{st}2}|$, respectively, are given in Fig. 15.

As shown, since the stator voltage changes continuously, the change pattern of $|\psi_{\mathrm{st}}|$ is obviously different from that of $|\psi_{\mathrm{sdc}}|$ during fault. When the proposed measurement method is implemented, $|\psi_{\mathrm{st}}|$ can be measured accurately during the whole commutation failure fault. Moreover, the delay time of the proposed measurement method is about 1.54 ms, which significantly improves the measure results compared with the traditional method.

The research work presented in [32] shows that the damping of the transient dc flux is decided by demagnetizing current and can be reflect by the stator short-circuit time constant τ. The increase in demagnetizing current will reduce τ, which means that the decay rate of transient dc flux will be accelerated. In the proposed continuous FRT control strategy, the rotor current reference can be rewritten as (22). Based on (22), it can be found that the demagnetizing current is decided by k_{de}. Consequently, the value of k_{de} will influence the effect on the damping of

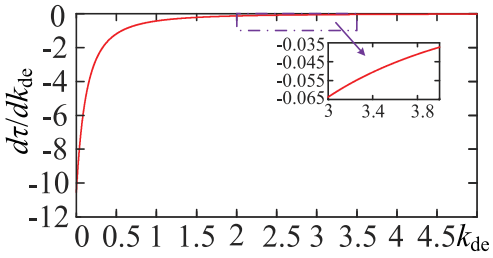

Fig. 16. Differential curve of τ.

transient dc flux

$$\boldsymbol{i}^{r}_{\mathrm{rref}} = -k_{de} \times \boldsymbol{\psi}^{r}_{st} = -k_{de} \times (\boldsymbol{\psi}^{r}_{sb} + \boldsymbol{\psi}^{r}_{sdc}). \tag{22}$$

In order to select the k_{de} reasonably during continuous FRT, $d\tau/dk_{\mathrm{de}}$ is given in (23). Besides, according to the parameters of the studied 2-MW DFIG listed in the Appendix, the curve of $d\tau/dk_{\mathrm{de}}$ is given in Fig. 16

$$\frac{d\tau}{dk_{de}} = \frac{-L_s L_m}{R_s(1 + L_m k_{de})^2}. \tag{23}$$

From Fig. 16, τ gradually decreases with the increase in k_{de}, and the larger the k_{de}, the smaller the change of τ. In Fig. 16, when k_{de} is set as 4, the decrease rate of τ is only -0.0373, which indicates that the increasing of k_{de} has a small influence on $\boldsymbol{\psi}^{s}_{\mathrm{sdc}}$.

In this article, with the consideration of the decay of $\boldsymbol{\psi}^{s}_{\mathrm{sdc}}$ and the rotor current limitation, the range of k_{de} is set as [2.5, 4]. When k_{de} is within this range, τ of the proposed control strategy is close to the traditional demagnetizing control strategy. Consequently, the effects of the two control strategies on the damping of the transient dc flux are similar to each other.

Furthermore, the grid codes require the DFIG to provide dynamic reactive power to support the power grid within tens of millisecond during fault [33], [34]. Therefore, in order to meet the requirements of the grid codes, the DFIG can be controlled to provide reactive power when the amplitude of rotor current is less than the rating value during commutation failure fault. According to (24), the rotor q-axis reactive current with the proposed control strategy can be calculated as follows:

$$|\boldsymbol{i}_{rqc}| = \begin{cases} 1 - |k_{de}\boldsymbol{\psi}_{st}| & 1 - |k_{de}\boldsymbol{\psi}_{st}| > 0 \\ 0 & 1 - |k_{de}\boldsymbol{\psi}_{st}| \le 0 \end{cases} \tag{24}$$

where the operator "| |" is the vector module.

In order to provide an enough dynamic reactive current and rapidly decay $\boldsymbol{\psi}^{s}_{\mathrm{sdc}}$ during fault, the product of $|\boldsymbol{i}_{\mathrm{rqc}}|$ and $1/\tau$ in (25) should be a large value. Therefore, k_{de} should be chosen for maximizing the product. In order to calculate k_{de}, which makes the product has the maximum value, the differential of (25) is given in (26)

$$m = \frac{R_s(1 + L_m k_{de})}{L_s}(1 - k_{de}\,|\boldsymbol{\psi}_{st}|) \tag{25}$$

$$\frac{dm}{dk_{de}} = \frac{R_s}{L_s} \times (L_m - 2L_m\,|k_{de}\boldsymbol{\psi}_{st}| - |\boldsymbol{\psi}_{st}|) \tag{26}$$

where m is the product of $|\boldsymbol{i}_{\mathrm{rqc}}|$ and $1/\tau$.

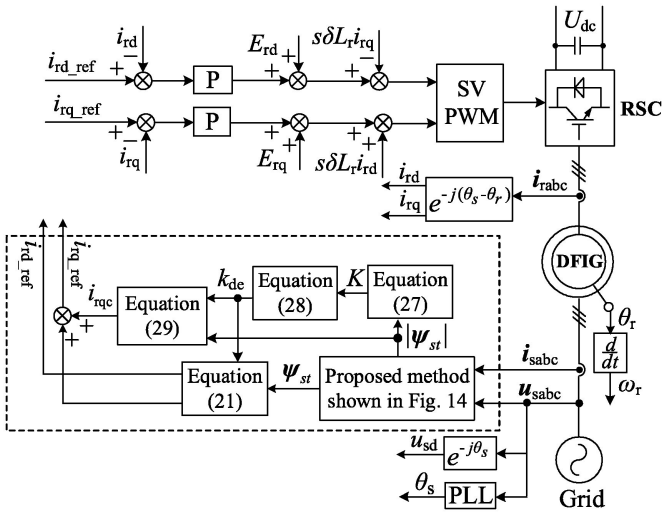

Fig. 17. Control diagram of the proposed continuous FRT strategy.

The k_{de}, which makes the product has the maximum value, can be calculated by setting (26) equals 0. As a result, the optimization value is given as

$$K = \frac{1}{2L_m}\left(\frac{L_m}{|\boldsymbol{\psi}_{st}|} - 1\right) \tag{27}$$

where K is the value that makes m has the maximum value.

Based on the analysis mentioned above, k_{de} and $\boldsymbol{i}_{\mathrm{rqc}}$ of the proposed control strategy can be calculated as (28) and (29), respectively. Meanwhile, combining with (21), the control diagram of the proposed continuous FRT strategy is shown in Fig. 17.

As can be seen, the features of the proposed continuous FRT control strategy include that $\boldsymbol{\psi}_{\mathrm{st}}$ rather than $\boldsymbol{\psi}_{\mathrm{sdc}}$ is introduced into the rotor current reference during fault and $\boldsymbol{\psi}_{\mathrm{st}}$ can be measured accurately and quickly under the stator voltage continuous changing condition. Besides, the control coefficient can be chosen reasonably, and DFIG can provide flexibly dynamic reactive current to support the transient grid voltage

$$k_{de} = \begin{cases} 2.5 & K < 2.5 \\ K & 2.5 \le K \le 4 \\ 4 & 4 < K \end{cases} \tag{28}$$

$$\boldsymbol{i}_{rqc} = \begin{cases} 1 - |k_{de}\boldsymbol{\psi}_{st}| & |\boldsymbol{i}_{rqc}| > 0 \text{ and } U_s < 0.9 \\ -(1 - |k_{de}\boldsymbol{\psi}_{st}|) & |\boldsymbol{i}_{rqc}| > 0 \text{ and } U_s > 1.1 \\ 0 & |\boldsymbol{i}_{rqc}| \le 0. \end{cases} \tag{29}$$

V. Simulation Results

In order to verify the proposed continuous FRT control strategy, the simulation has been done in Matlab/Simulink. The parameters of the simulation are listed in the Appendix, and the structure of the 2-MW DFIG system is shown in Fig. 18.

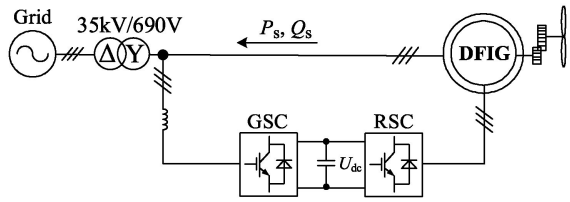

Fig. 18. Structure of the 2-MW DFIG system.

A. Commutation Failure Fault

Initially, the DFIG works at the rated voltage, and s is -0.2. The active power and the reactive power of DFIG are set as 0.8 and 0 p.u., respectively. Additionally, in order to compare the overcurrent suppression abilities of the proposed FRT control strategy and the traditional demagnetizing control strategy, once the fault is detected, the FRT control strategies are enabled until the conventional vector control (VC) strategy is reactivated after 200 ms.

1) Slight Commutation Failure Fault: The performances of the proposed continuous FRT control strategy and the traditional demagnetizing control strategy under slight commutation failure fault are given in Fig. 19. As shown in the figure, the control coefficient of the traditional demagnetizing control strategy is set as 3, according to [21]. Fig. 20 shows the key variable waveforms of the two control strategies.

As shown in Fig. 19, both the control strategies can restrict the rotor current within the rated value under slight commutation failure. Meanwhile, due to ψ_{sb}, $|\psi_{st}|$ has a significant change during commutation failure shown in Fig. 20, which is totally different from the traditional transient dc flux response. Moreover, ψ_{st} can be measured accurately and quickly with the proposed measurement method. However, compared with the proposed method, there is a big error between $|\psi_{st1}|$ and $|\psi_{st}|$. The maximum error is about 21.4%. Besides, when the proposed continuous FRT control strategy is adopted, k_{de} changes within the limitation value. The large $|\psi_{st}|$ will decrease k_{de}, and the small $|\psi_{st}|$ will increase k_{de}. As a result, the transient dc flux can be quickly decayed, and the DFIG can provide dynamic reactive current according to the operation status of the DFIG system to support the connected grid during slight commutation failure. This indicates that the DFIG can be controlled more flexible, and the FRT performance can be enhanced as well. Moreover, it can be found that $|\psi_{st1}|$ is close to $|\psi_{st2}|$ when the stator voltage is constant at $t = 3.11$ s. Since ψ_{st} is equal to ψ_{sdc} when the stator voltage is constant, the simulation results show that the proposed control strategy has an effect similar to the demagnetizing control strategy on the damping of the transient dc flux. After $t = 3.2$ s, the DFIG can recover to the normal operation condition when the conventional VC is reactivated.

2) Severe Commutation Failure Fault: Fig. 21 shows the simulation results under severe commutation failure. In order to compare the overcurrent suppression ability between the proposed continuous FRT control strategy and the traditional demagnetizing control strategy, the control coefficient of the traditional demagnetizing control strategy is set as 2.5. Fig. 22 shows the key variable waveforms of the proposed continuous FRT control strategy and the demagnetizing control strategy.

As can be seen from Figs. 21 and 22, when the proposed control strategy is adopted, the rotor current is effectively limited within the generally stated maximum of insulated gate bipolar

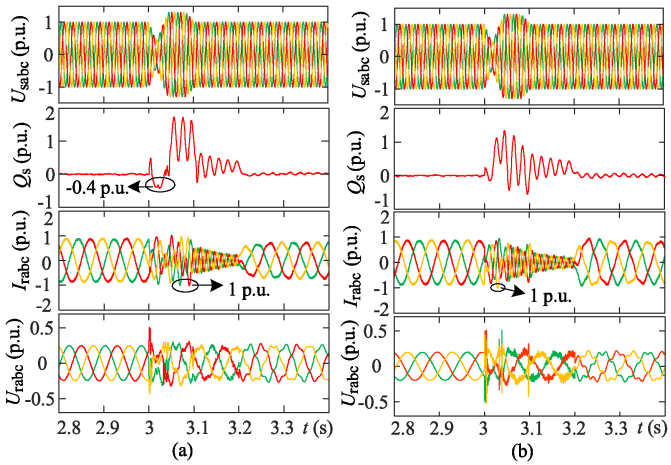

Fig. 19. Simulation results under slight commutation failure fault. (a) Proposed continuous FRT control strategy. (b) Demagnetizing control strategy.

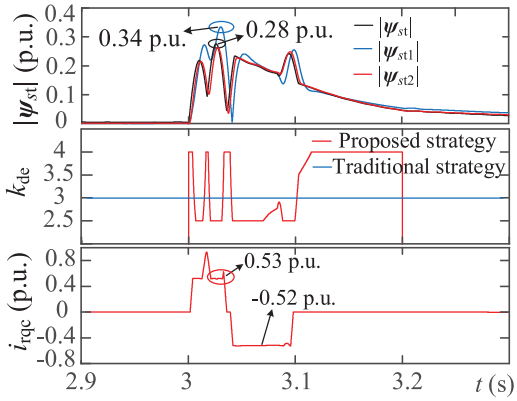

Fig. 20. Key variable waveforms of the proposed control strategy and the demagnetizing control strategy under slight commutation failure.

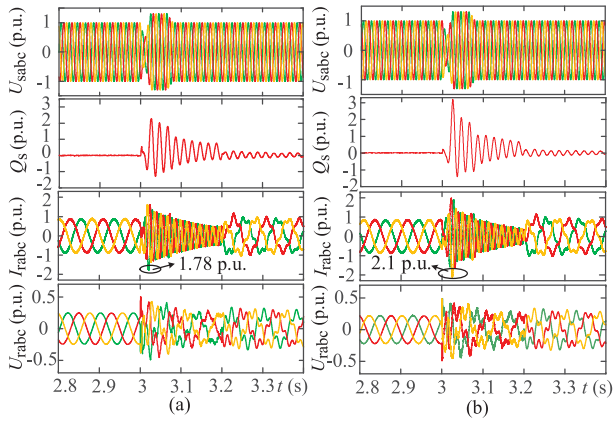

Fig. 21. Simulation results under severe commutation failure fault. (a) Proposed continuous FRT control strategy. (b) Demagnetizing control strategy.

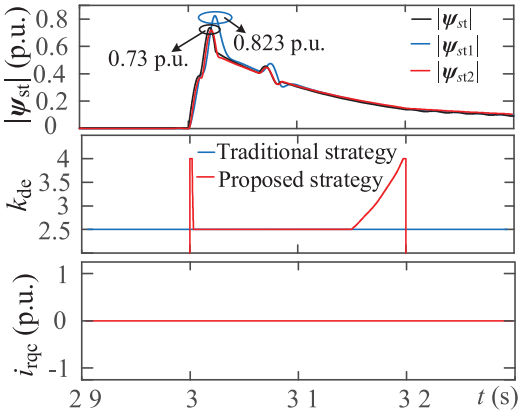

Fig. 22. Key variable waveforms of the proposed control strategy and the demagnetizing control strategy under severe commutation failure.

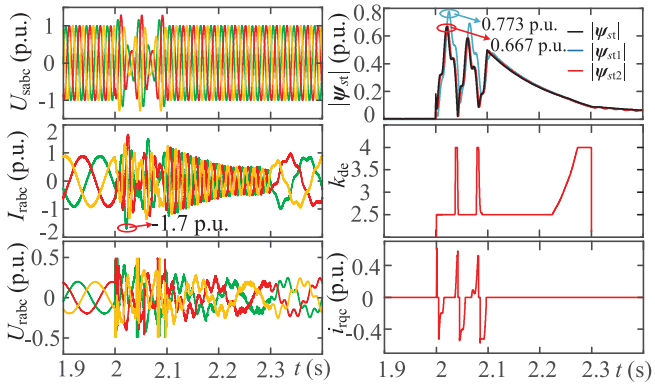

Fig. 23. Simulation results of the proposed continuous FRT control strategy when the stator voltage continuously changes.

transistor (IGBT) pulse current of 2.0 p.u. [35]. Meanwhile, since the amplitude of $|\psi_{st}|$ is at a large value, the dynamic reactive current is 0 p.u. during fault, and k_{de} is equal to 2.5 before $t = 3.15$ s. After 3.15 s, k_{de} increases fast for small $|\psi_{st}|$. At $t = 3.2$ s, the traditional VC is enabled, and the DFIG can recover to the normal operation. However, when the traditional demagnetizing control strategy is adopted, there is a significant error between $|\psi_{st1}|$ and $|\psi_{st}|$. The maximum error is about 12.7% of $|\psi_{st}|$. As a result, the maximum rotor overcurrent amplitude under the control of the traditional demagnetizing control strategy is up to 2.1 p.u., which exceeds the current limitation of RSC and destroy the DFIG system. As mentioned above, the proposed continuous FRT control strategy has a better overcurrent suppression ability than the traditional demagnetizing control strategy under the stator voltage continuous changing condition. Additionally, from Fig. 22, $|\psi_{st1}|$ is also close to $|\psi_{st2}|$ when the stator voltage is constant at $t = 3.088$ s, which shows that the proposed control strategy has an effect similar to the demagnetizing control strategy on the damping of the transient dc flux.

B. Continuously Changing Stator Voltage

The proposed continuous FRT control strategy is not only suitable for the commutation failure, but also for the scenarios with the continuous voltage variation condition. In order to validate the generality of the proposed continuous FRT control strategy, the following simulation has been done, and the results are given in Fig. 23.

Initially, the DFIG works at the rated voltage, and s is -0.2. The active power and the reactive power of DFIG stator are set as 0.8 p.u. and 0 p.u., respectively. Once the fault is detected, the proposed continuous FRT control strategy is enabled until the conventional VC strategy is reactivated after 200 ms. Meanwhile, the stator voltage of DFIG is set as (30) in this simulation. Based on (30), it can be found that the stator voltage changes continuously during the fault, which can represent the typically continuous stator voltage variation condition

$$\boldsymbol{U}_s^s = \begin{cases} \boldsymbol{U}_{sN}^s & t < 2 \text{ s} \\ [0.5 \times \sin(50p \times t) + 0.8] \times \boldsymbol{U}_{sN}^s & 2 \text{ s} \le t \le 2.1 \text{ s} \\ \boldsymbol{U}_{sN}^s & 2.1 \text{ s} < t. \end{cases} \tag{30}$$

As can be seen from Fig. 23, when the proposed continuous FRT control strategy is adopted during the fault, the rotor current can be well controlled, and the maximum rotor current amplitude is 1.7 p.u., which is within 2 p.u. Meanwhile, the proposed control strategy can measure ψ_{st} accurately and quickly when the stator voltage continuously changes, which indicates that the proposed control strategy is general to the scenarios with the continuous voltage variation condition. Additionally, the k_{de} changes according to the operation state of DFIG, and the DFIG can provide appropriate reactive current to support the connected power grid. The simulation results given in Fig. 23 validate the effectiveness and the superiority of the proposed continuous FRT control strategy under the continuous voltage variation condition.

C. Stator Voltage Drop Fault

The performances of the proposed continuous FRT control strategy under stator voltage drop fault are also simulated for validating the effectiveness. Initially, the DFIG are controlled by VC strategy and works at rated voltage. The output active power and reactive power of DFIG stator are 0.8 and 0 p.u., respectively, and s is -0.2. At $t = 3$ s, a symmetrical fault with an 80% depth of voltage dip occurs at the DFIG stator, and the fault is cleared at $t = 3.2$ s. Once the fault is detected, the proposed continuous FRT control strategy is activated until the VC strategy is enabled at $t = 3.4$ s. The simulation results are given in Fig. 24.

Based on Fig. 24, it can be seen that the rotor current can be effectively suppressed within 2 p.u. The simulation results given in Fig. 24 show that the proposed control strategy can realize the FRT control of DFIG during severe stator voltage drop, which nicely demonstrate the analysis presented in Section IV.

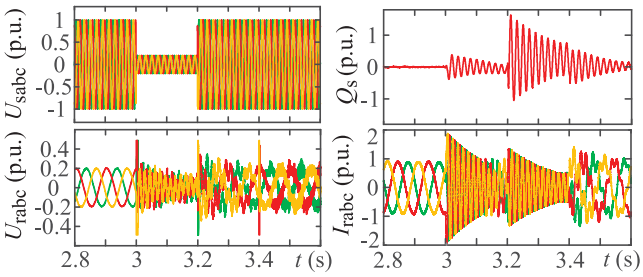

Fig. 24. Simulation results of the proposed commutation failure FRT control strategy under severe stator voltage drop fault.

In summary, the proposed continuous FRT control strategy has the following advantages compared with the existing FRT control strategies.

1) In the proposed control strategy, ψ_{st} rather than ψ_{sdc} is introduced into the rotor current reference. Besides, the measurement method that can measure ψ_{st} accurately and quickly is proposed. Consequently, the proposed continuous FRT control strategy has a better overcurrent suppression ability than the existing FRT control strategies under the stator voltage continuous changing condition.
2) During fault, the control coefficient of the proposed control strategy can be chosen reasonably according to the operation status of DFIG system. As a result, the transient dc flux is decayed quickly, and the DFIG can provide dynamic reactive current to support the connected power grid, which means that the DFIG system can achieve a more flexible and enhanced FRT operation.
3) The proposed continuous FRT control strategy is general to the scenarios with the continuous voltage variation condition and not limited to the commutation failure situation.

VI. Experimental Results

In order to validate the effectiveness of the proposed control strategy, the experimental tests were performed on a laboratory-scale DFIG system. The schematic diagram is shown in Fig. 18, and the setup of the experimental system is shown in Fig. 25. Moreover, the detailed electrical parameters of the laboratory-scale DFIG system are given in the Appendix. The DFIG is derived by a dc motor. The RSC and grid side converter (GSC) are controlled by TI Digital Signal Processor (TMS320F28335). The switching frequency and the sampling frequency for both converters are set to 10 kHz. The stator voltage of the DFIG system is generated by using the Chroma 61830 Regenerative Grid Simulator, which can be programmed to set different voltage waveforms.

A. Commutation Failure Fault

Initially, DFIG is controlled under conventional VC, and the active power and reactive power of DFIG are 0.8 and 0 p.u., respectively. Once the fault occurs, the proposed control strategy is activated. When the fault is cleared, the VC is reactivated after 200 ms. In addition, s is -0.1 in the experiment.Fig. 26(a) and

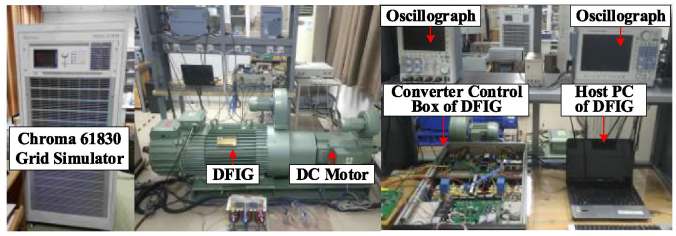

Fig. 25. Setup of experimental system.

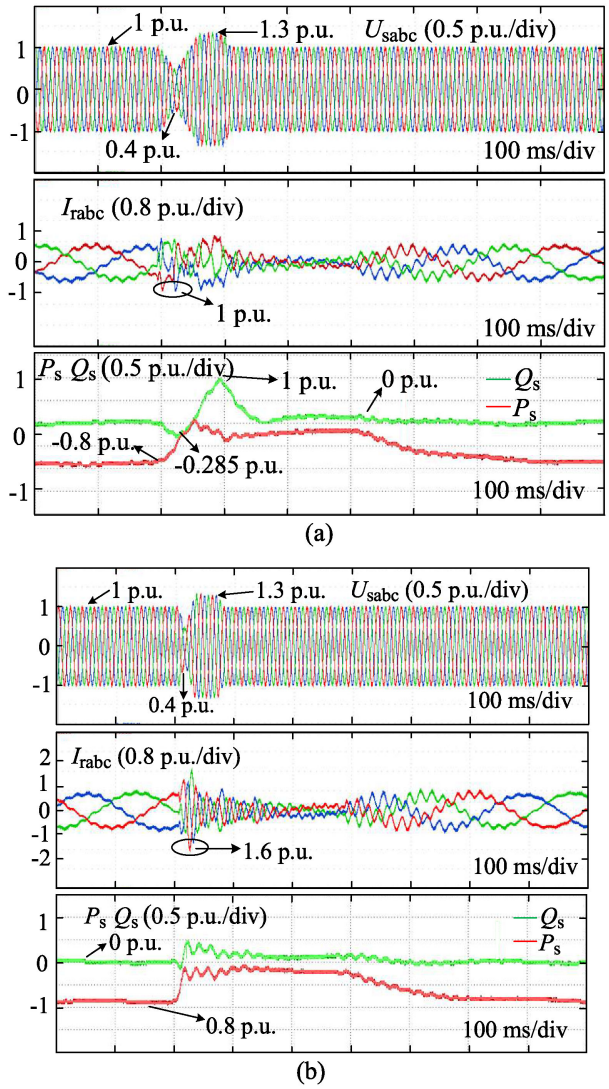

Fig. 26. Experimental results for commutation failure ride through. (a) Experimental results under slight commutation failure fault. (b) Experimental results under severe commutation failure fault.

(b) shows the experimental results with the slight commutation failure and severe commutation failure, respectively.

From Fig. 26(a), it can be seen that when the proposed continuous FRT control strategy is adopted, the rotor current is well restricted within the rating value during the slight commutation failure. Meanwhile, the DFIG can be controlled to provide dynamic reactive current to support the power grid. The output

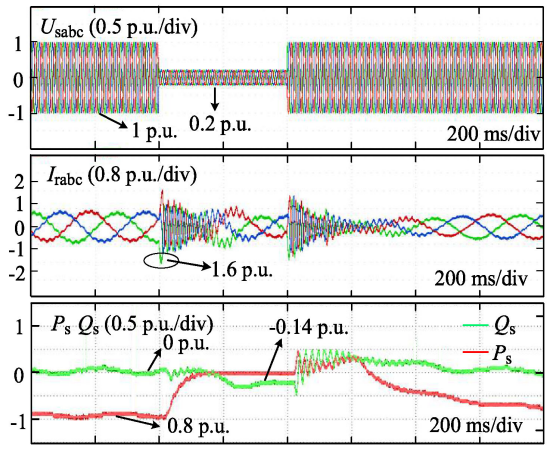

Fig. 27. Experimental results under severe voltage drop fault.

maximum reactive power is equal to 0.285 p.u., whereas the absorbed maximum reactive power is equal to 1 p.u. From Fig. 26(b), when the proposed continuous FRT control strategy is adopted under severe commutation failure, the dynamic reactive current is equal to 0 p.u. due to the large $|\psi_{\rm st}|$. Furthermore, the maximum rotor current amplitude is 1.6 p.u., which is quite a few from the current limitation of RSC. Consequently, the overcurrent protection will not be triggered, and the DFIG can stay in the grid, which shows that the proposed continuous FRT control strategy has a great FRT performance under the stator voltage continuous changing condition. Meanwhile, when the VC is reactivated, the DFIG recovers to the normal operation status.

B. Stator Voltage Drop Fault

Under a typically severe stator voltage drop fault, the FRT experiment also has been done, and the experimental results are given in Fig. 27. It can be seen from Fig. 27 that the maximum rotor current amplitude is 1.6 p.u. when the proposed continuous FRT control strategy is adopted, which shows that the proposed control strategy also has a very nice LVRT performance. Meanwhile, with the dynamic reactive current injection, the output maximum reactive power of DFIG is 0.14 p.u. The results shown in Fig. 27 indicate that the proposed control strategy is also suitable for the traditional severe stator voltage drop fault.

Similar to the simulation results, the experimental results also demonstrate that the proposed continuous FRT control strategy is general for the scenarios with the continuous voltage variation condition, which provides a novel method for the FRT operation of the DFIG system.

VII. Conclusion

During commutation failure in the LCC-HVdc transmission system, the stator voltage of the grid-connected DFIG in the sending ac system changes continuously and presents the "first reduce then rise" characteristic, which may trip off the connected DFIG-based wind turbine. In this article, the stator flux and EMF of DFIG when the stator voltage changes continuously are analyzed for the first time. The analysis shows that the stator flux component ignored in the previous works has the same contribution to the EMF as the transient dc flux. Furthermore, an improved continuous FRT control strategy of DFIG is proposed, and the control coefficient of the proposed strategy is designed as well. Based on the simulation and experiment, when the proposed control strategy is adopted, the overcurrent suppression ability of the DFIG can be further improved under the stator voltage continuous changing condition. Furthermore, since the control coefficient is chosen reasonably, the transient dc flux is decayed quickly, and the DFIG can provide dynamic reactive current to support the power grid, which means that the DFIG can achieve a more flexible and enhanced FRT operation. Additionally, it is worth noting that although this article is researched based on the commutation failure condition, the proposed continuous FRT control strategy is general to the scenarios with the continuous voltage variation condition.

Appendix

A. Simulation Parameters of LCC-HVDC Transmission System

The following are the DFIG-based wind farm parameters.

1) Ratings: $S_n = 50 \times 2$ MW, $f_n = 50$ Hz, $U_n = 690$ V (line-to-line rms), $V_{\rm dc} = 1200$ V.
2) Stator and rotor resistors: $R_s = 0.022$ p.u., $R_r = 0.016$ p.u.
3) Stator and rotor leakage inductances: $L_{\sigma s} = 0.173$ p.u., $L_{\sigma r} = 0.16$ p.u.
4) Mutual inductance: $L_m = 2.78$ p.u.
5) Reactor: $L_g = 0.008$ mH.
6) DC-link capacitor: $C = 50 \times 14$ mF.

The following are the LCC-HVdc system parameters.

1) Ratings: $P_n = 1200$ MW, $U_{\rm dc} = \pm 500$ kV
2) Rating voltage of sending ac bus: $V_{sn} = 345$ kV
3) Rating voltage of receiving ac bus: $V_{rn} = 500$ kV
4) Rating capacity of VAR compensator: $Q_n = 320$ Mvar

The following are the simulation parameters of the 2-MW DFIG system.

1) Ratings: $S_n = 2$ MW, $f_n = 50$ Hz, $U_n = 690$ V (line-to-line rms), $V_{\rm dc} = 1200$ V.
2) Stator and rotor resistors: $R_s = 0.022$ p.u., $R_r = 0.016$ p.u.
3) Stator and rotor leakage inductances: $L_{\sigma s} = 0.173$ p.u., $L_{\sigma r} = 0.16$ p.u.
4) Mutual inductance: $L_m = 2.78$ p.u.
5) Reactor: $L_g = 0.003$ mH.
6) DC-link capacitor: $C = 14$ mF.
7) Pairs of poles: 2.
8) Turn ratio: $N_s/N_r = 0.4$.

The following are the experimental parameters of the 2-kW DFIG system.

1) Ratings: $S_n = 2$ kW, $f_n = 50$ Hz, $U_n = 220$ V (line-to-line rms), $V_{\rm dc} = 400$ V.
2) Stator and rotor resistors: $R_s = 1.09\ \Omega$, $R_r = 1.55\ \Omega$
3) Stator and rotor leakage inductances: $L_{\sigma s} = 2$ mH, $L_{\sigma r} = 4.36$ mH
4) Mutual inductance: $L_m = 64.6$ mH
5) Reactor: $L_g = 4$ mH
6) DC-link capacitor: $C = 1100\ \mu$F
7) Pairs of poles: 2
8) Turn ratio: $N_s/N_r = 0.517$

REFERENCES

[1] L. Wang and M. S.-N. Thi, "Stability enhancement of large-scale integration of wind, solar, and marine-current power generation fed to an SG-based power system through an LCC-HVDC link," *IEEE Trans. Sustain. Energy*, vol. 5, no. 1, pp. 160–170, Sep. 2013.

[2] H. P. Yin, L. L. Fan, and Z. X. Miao, "Fast power routing through HVDC," *IEEE Trans. Power Del.*, vol. 27, no. 3, pp. 1432–1441, Jun. 2012.

[3] H. J. Lee, G. T. Son, J.-I. Yoo, and J.-W. Park, "Effect of a SFCL on commutation failure in a HVDC system," *IEEE Trans. Appl. Supercond.*, vol. 23, no. 3, pp. 1–4, Jun. 2013.

[4] W. Peng, L. Jian-Kun, Z. Qian, and Z. Ning-Yu, "Research on commutation failure of Jinsu DC transmission project caused by a complex AC fault," *J. Eng.*, vol. 2019, no. 16, pp. 775–778, Apr. 2019.

[5] J. Z. Tu *et al.*, "Mechanism analysis and control measures of wind turbine generators tripping caused by HVDC contingencies," in *Proc. 12th IET Int. Conf. AC DC Power Transmiss.*, Beijing, China, 2016, pp. 1–7.

[6] Y. M. Alsmadi *et al.*, "Detailed investigation and performance improvement of the dynamic behavior of grid-connected DFIG-based wind turbines under LVRT conditions," *IEEE Trans. Ind. Appl.*, vol. 54, no. 5, pp. 4795–4812, May 2018.

[7] C. Y. Guo, Y. Liu, C. Zhao, X. Wei, and W. Xu, "Power component fault detection method and improved current order limiter control for commutation failure mitigation in HVDC," *IEEE Trans. Power Del.*, vol. 30, no. 3, pp. 1585–1593, Jun. 2015.

[8] S. Mirsaeidi, X. Dong, D. Tzelepis, D. M. Said, A. Dyśko, and C. Booth, "A predictive control strategy for mitigation of commutation failure in LCC-based HVDC systems," *IEEE Trans. Power Electron.*, vol. 34, no. 1, pp. 160–172, Jan. 2019.

[9] Y. Xue, X. P. Zhang, and C. H. Yang, "Commutation failure elimination of LCC HVDC systems using thyristor-based controllable capacitors," *IEEE Trans. Power Del.*, vol. 33, no. 3, pp. 1448–1458, Dec. 2017.

[10] Y. Xue, X. P. Zhang, and C. H. Yang, "Elimination of commutation failures of LCC HVDC system with controllable capacitors," *IEEE Trans. Power Syst.*, vol. 31, no. 4, pp. 3289–3299, Jul. 2016.

[11] C. Y. Guo, Z. Yang, B. Jiang, and C. Zhao, "An evolved capacitor-commutated converter embedded with antiparallel thyristors based dual-directional full-bridge module," *IEEE Trans. Power Del.*, vol. 33, no. 2, pp. 928–937, Apr. 2018.

[12] Y. Xue, X. P. Zhang, and C. H. Yang, "Commutation failure elimination of LCC HVDC systems using thyristor-based controllable capacitors," *IEEE Trans. Power Del.*, vol. 33, no. 3, pp. 1448–1458, Dec. 2017.

[13] Q. Q. Zheng *et al.*, "A STATCOM compensation scheme for suppressing commutation failure in HVDC," in *Proc. 42nd Annu. Conf. IEEE Ind. Electron. Soc.*, Florence, Italy, 2016, pp. 1–6.

[14] Q. Wang, T. Li, X. Tang, F. Liu, and J. Lei, "Study on the site selection for synchronous condenser responding to commutation failures of multi-infeed HVDC system," *J. Eng.*, vol. 2019, no. 16, pp. 1413–1418, Apr. 2019.

[15] Y. Z. Sun, L. Peng, F. Ma, G. J. Li, and P. F. Lv, "Design a fuzzy controller to minimize the effect failure on power system," *IEEE Trans. Power Del.*, vol. 23, no. 1, pp. 100–107, Jan. 2008.

[16] Z. N. Wei, Y. Yuan, X. Lei, H. Wang, G. Sun, and Y. Sun, "Direct-current predictive control strategy for inhibiting commutation failure in HVDC converter," *IEEE Trans. Power Del.*, vol. 29, no. 5, pp. 2409–2417, Feb. 2014.

[17] L. D. Zhang and L. Dofnas, "A novel method to mitigate commutation failures in HVDC systems," in *Proc. Int. Conf. Power Syst. Technol.*, Kunming, China, 2002, pp. 1–6.

[18] W. Yao, C. Liu, J. Fang, X. Ai, J. Wen, and S. Cheng, "Probabilistic analysis of commutation failure in LCC-HVDC system considering the CFPREV and the initial fault voltage angle," *IEEE Trans. Power Del.*, vol. 35, no. 2, pp. 715–724, Apr. 2020.

[19] S. Mirsaeidi and X. Z. Dong, "An enhanced strategy to inhibit commutation failure in line-commutated converters," *IEEE Trans. Ind. Electron.*, vol. 67, no. 1, pp. 340–349, Jan. 2020.

[20] X. D. Zou, D. Zhu, J. Hu, S. Zhou, and Y. Kang, "Mechanism analysis of the required rotor current and voltage for DFIG-based WTs to ride-through severe symmetrical grid faults," *IEEE Trans. Power Electron.*, vol. 33, no. 9, pp. 7300–7304, Sep. 2018.

[21] D. Zhou and F. Blaabjerg, "Optimized demagnetizing control of DFIG power converter for reduced thermal stress during symmetrical grid fault," *IEEE Trans. Power Electron.*, vol. 33, no. 12, pp. 10326–10340, Dec. 2018.

[22] D. H. Zhu, X. Zhu, L. Zou, Q. Deng, S. Huang, and Y. Kang, "Inductance-emulating control for DFIG-based wind turbine to ride-through grid faults," *IEEE Trans. Power Electron.*, vol. 32, no. 11, pp. 8514–8525, Nov. 2017.

[23] Q. J. Huang, X. Zou, D. Zhu, and Y. Kang, "Scaled current tracking control for doubly fed induction generator to ride-through serious grid faults," *IEEE Trans. Power Electron.*, vol. 31, no. 3, pp. 2150–2165, Mar. 2016.

[24] R. W. Zhu, Z. Chen, X. Wu, and F. Deng, "Virtual damping flux-based LVRT control for DFIG-based wind turbine," *IEEE Trans. Energy Convers.*, vol. 30, no. 2, pp. 714–725, Jun. 2015.

[25] Z. Xie, X. Zhang, X. Zhang, S. Yang, and L. Wang, "Improved ride-through control of DFIG during grid voltage swell," *IEEE Trans. Ind. Electron.*, vol. 62, no. 6, pp. 3584–3594, Jun. 2015.

[26] S. L. Li, Q. Shiyao, W. Ruiming, Y. Xuesong, and D. Linwang, "Study on voltage withstand characteristics and HVRT control strategy for DFIG wind turbines," in *Proc. Int. Conf. Power Syst. Technol.*, Guangzhou, China, 2018, pp. 1–7.

[27] CIGRE/CIRED/UIE JWG C4.110, Voltage Dip Immunity of Equipment and Installations," CIGRE Technical Brochure TB 412, Apr. 2010. [Online]. Available: http://www.e-cigre.org or http://www.uie.org

[28] M. Szechtma, T. Wess and C.V. Thio, "A benchmark model for HVDC system studies," in *Proc. Int. Conf. AC DC Power Transmiss.*, London, U.K., 1991, pp. 1–5.

[29] C. Q. Wang, C. Zhang, X. Kong, P. Li, and Y. Yuan, "Procedure analysis of UHVDC commutation failure," *J. Eng.*, vol. 2019, no. 16, pp. 3132–3134, 2019.

[30] M. J. Han, J. Wen, and Y. H. Xu, "Harmonic suppression and reactive power compensation of LCC-HVDC," in *The Principle and Operation of HVDC Transmission*. Beijing, China: China Elect. Power Press, 2012, pp. 131–132.

[31] J. Z. Tu, Y. Pan, J. Zhang, B. Zeng, J. Jia, and J. Yi, "Transient reactive power characteristics of HVDC during commutation failure and impact of HVDC control parameters," *J. Eng.*, vol. 2017, no. 13, pp. 1134–1139, 2017.

[32] Q. J. Huang, X. D. Zou, and L. Tong, "Analysis of the electromagnetic transient time in DFIG during grid faults," in *Proc. IEEE Appl. Power Electron. Conf. Expo.*, Fort Worth, TX, USA, 2014, pp. 1–6.

[33] *Technical Rule for Connecting Wind Farm to Power System*, Chinese Standard GB/T 19963-2011, China Electric Power Press, Beijing, China, 2011.

[34] *Grid Code High and Extra High Voltage*, Germany Standard, E. ON. Netz GmbH, Bayreuth, German, Apr. 2006.

[35] Y. Chang, J. Hu, and X. Yuan, "Mechanism analysis of DFIG-based wind turbine's fault current during LVRT with equivalent inductances," *IEEE J. Emerg. Sel. Topics Power Electron.*, vol. 8, no. 2, pp. 1515–1527, Jun. 2020.

Tian Zhang received the B.Eng. degree in electrical engineering and automation from Zhengzhou University, Henan, China, in 2017. He is currently working toward the M.Sc. degree with the School of Electrical Engineering, Chongqing University, Chongqing, China.

His research interests include high-voltage direct current transmission, control of wind turbine generation system, and renewable power generation.

Jun Yao (Member, IEEE) received the B.Eng., M.Sc., and Ph.D. degrees from Chongqing University, Chongqing, China, in 2001, 2004, and 2007, respectively, all in electrical engineering.

Since 2004, he has been with the School of Electrical Engineering, Chongqing University, where he is currently a Professor. He was a Visiting Researcher with the Department of Energy Technology, Aalborg University, Aalborg, Denmark, from 2012 to 2013. He has authored/coauthored more than 90 peer-reviewed technical papers and holds more than 20 issued/pending patents. His research interests include electric machines control, power electronics conversion and control, and renewable power generation. His main current research interests include wind energy and power electronics application to the power systems.

Dr. Yao is a member of the IEC TC 8/SC 8A/JWG5.

Peng Sun received the B.Eng. degree in electrical engineering and automation from Anhui University, Hefei, China, in 2017. He is currently working toward the Ph.D. degree in the School of Electrical Engineering, Chongqing University, Chongqing, China.

His research interests include electric machines control, modeling and control of wind turbine generation system, and renewable power generation.

Jinxin Pei received the B.Eng. degree in electrical engineering and automation from Henan Polytechnic University, Jiaozuo, China, in 2016. He is currently working toward the Ph.D. degree with the College of Electrical Engineering, Chongqing University, Chongqing, China.

His research interests include electric machines control, modeling and control of wind turbine generation system, and renewable power generation.

Hailin Zhang (Member, IEEE) was born in Chongqing, China. He received the B.E., M.E., and Ph.D. degrees in electrical engineering from the Harbin Institute of Technology, Harbin, China, in 2010, 2012, and 2017, respectively.

He is currently a Postdoctoral Researcher with the Postdoctoral Station of Electrical Engineering, Chongqing University, Chongqing, China. His research interests include soft-switching converters, high-precision motor drive, and renewable power generation.

Kai Liu received the B.Eng. degree in electrical engineering and automation from Nanchang University, Nanchang, China, in 2018. He is currently working toward the M.Sc. degree with the School of Electrical Engineering, Chongqing University, Chongqing, China.

His research interests include electric machines control, high-voltage dc technology, and stability analysis of power systems with renewable energy generations.

Yang Zhao received the B.Eng. degree in ship electronic and electrical engineering from Dalian Maritime University, Dalian, China, in 2018. He is currently working toward the M.Sc. degree with the School of Electrical Engineering, Chongqing University, Chongqing, China.

His research interests include electric machines control, modeling and control of wind turbine generation system, and renewable power generation.